AGU PUBLICATIONS

JGR

Journal of Geophysical Research: Solid Earth

RESEARCH ARTICLE
10.1002/2015JB012060

Key Points:
- Abrupt shut-in can lead to locally sharp increase in seismicity rate
- Tapering injection rate mitigates postinjection increase
- In low-stress environments the largest event may occur postinjection

Correspondence to:
P. Segall,
segall@stanford.edu

Citation:
Segall, P., and S. Lu (2015), Injection-induced seismicity: Poroelastic and earthquake nucleation effects, *J. Geophys. Res. Solid Earth*, *120*, 5082–5103, doi:10.1002/2015JB012060.

Received 26 MAR 2015
Accepted 24 MAY 2015
Accepted article online 30 MAY 2015
Published online 16 JUL 2015

Injection-induced seismicity: Poroelastic and earthquake nucleation effects

P. Segall[1] and S. Lu[2]

[1]Department of Geophysics, Stanford University, Stanford, California, USA, [2]Institute for Computational and Mathematical Engineering, Stanford University, Stanford, California, USA

Abstract The standard model of injection-induced seismicity considers changes in Coulomb strength due solely to changes in pore pressure. We consider two additional effects: full poroelastic coupling of stress and pore pressure, and time-dependent earthquake nucleation. We model stress and pore pressure due to specified injection rate in a homogeneous, poroelastic medium. Stress and pore pressure are used to compute seismicity rate through the Dieterich (1994) model. For constant injection rate, the time to reach a critical seismicity rate scales with $t \sim r^2/(cf_c)$, where r is distance from the injector, c is hydraulic diffusivity, and f_c is a factor that depends on mechanical properties, and weakly on r. The seismicity rate decays following a peak, consistent with some observations. During injection poroelastic coupling may increase or decrease the seismicity rate, depending on the orientation of the faults relative to the injector. If injection-induced stresses inhibit slip, abrupt shut-in can lead to locally sharp increases in seismicity rate; tapering the flux mitigates this effect. The maximum magnitude event has been observed to occur postinjection. We suggest the seismicity rate at a given magnitude depends on the nucleation rate, the size distribution of fault segments, and if the background shear stress is low, the time-varying volume of perturbed crust. This leads to a rollover in frequency-magnitude distribution for larger events, with a "corner" that increases with time. Larger events are absent at short times, but approach the background frequency with time; larger events occurring post shut-in are thus not unexpected.

1. Introduction

Injection-induced seismicity has been known since the earthquakes triggered at the Rocky Mountain Arsenal [*Healy et al.*, 1968] and the subsequent experiment in earthquake control at Rangely [*Raleigh et al.*, 1976]. More recently, the subject has gained widespread attention due to earthquakes apparently triggered by waste water injection [e.g., *Horton*, 2012; *Kim*, 2013; *Keranen et al.*, 2014] and geothermal operations [e.g., *Baisch et al.*, 2010; *Deichmann and Giardini*, 2009]. Recent reviews of the subject include those by *Ellsworth* [2013] and *National Research Council* [2013].

Since the pioneering study at the Rangely oil field [*Raleigh et al.*, 1976] the mechanism for inducing earthquakes has been understood to be increasing pore pressure reducing the effective normal stress acting across preexisting fault surfaces. This reduces the shear resistance, allowing slip under ambient tectonic shear stresses. Much of the analysis on induced seismicity has thus focussed on modeling the diffusion of pore pressure due to injection [e.g., *Hsieh and Bredehoeft*, 1981; *Zhang et al.*, 2013].

At the same time, there is also convincing evidence that production induced declines in pore pressure can induce earthquakes near oil and gas fields [*Segall*, 1989; *Suckale*, 2009]. The mechanism for this is understood to be that decreased pore pressures cause poroelastic changes in solid stress that under appropriate conditions can lead to earthquakes [*Segall*, 1989; *Segall et al.*, 1994]. Nearly all studies of injection-induced seismicity ignore poroelastic effects; the assumption, either implicit or explicit, being that direct pore pressure changes are the dominant effect in destabilizing faults. Exceptions to this include *Rutqvist et al.* [2008] and *Rozhko* [2010]. *Rozhko* [2010] considered one-way coupling of pore pressure and stress, and recognized that shear stress changes may dominate over changes in pore pressure at points relatively far from the injector. In the full theory of poroelasticity, changes in pore pressure induce stresses, while changes in mean normal stress induce changes in pore pressure [*Biot*, 1941; *Rice and Cleary*, 1976; *Wang*, 2000]. One goal of this work is to explore the effect of full poroelastic coupling on injection-induced seismicity for a simple geometry with a point injector and homogeneous hydraulic and mechanical properties.

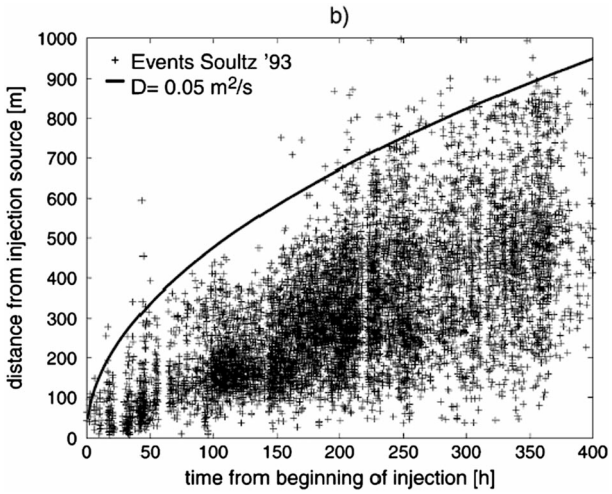

Figure 1. Time distance plot for seismicity from the 1993 injection at Soultz-sous-Forêts. Curve shows $r = \sqrt{Dt}$ where the value of the diffusivity D is indicated. From *Shapiro et al.* [2002].

Another effect that is widely ignored in the literature on induced seismicity is the intrinsic time dependence of earthquake nucleation. Both laboratory data and models based on rate-state friction show that time to dynamic instability depends on both initial conditions and applied stress [*Dieterich and Kilgore*, 1996]. Most studies of induced earthquakes assume the space-time evolution of seismicity is controlled solely by the diffusion of pore pressure, and that fault slip occurs as soon as a critical Coulomb stress condition is met. Thus, researchers fit diffusion profiles of the form $r = \sqrt{ct}$ to the onset of seismicity (Figure 1), where c is hydraulic diffusivity. The second goal of this study is to examine how the intrinsic rate dependence in earthquake nucleation together with pore pressure and stress diffusion influences the spatiotemporal evolution of induced seismicity. In particular, we address the question of whether the onset of seismicity can still be fit with a diffusion profile when both poroelastic and time-dependent nucleation effects are included.

It is widely observed that earthquakes continue after injection has stopped, and it is not uncommon for the largest earthquake to occur after injection has ceased. This was observed following waste water injection in Youngstown, Ohio [*Kim*, 2013], and due to geothermal operations in Basel, Switzerland [*Deichmann and Giardini*, 2009], and Soultz-sous-Forêts, France [*Dorbath et al.*, 2009]. This presents a particularly challenging problem for operators as terminating injection does not ensure that larger events will not follow. There has been some research on this problem from both statistical [e.g., *Barth et al.*, 2013; *Shapiro et al.*, 2013] and mechanical perspectives [e.g., *Baisch et al.*, 2010]. Our analysis sheds light on this problem by revealing physical effects that control the magnitude of post-injection events.

Here we examine the predicted response to injection into a mechanically and hydraulically homogeneous medium, but include the effects of poroelastic coupling and time-dependent nucleation. Section 2 reviews the poroelastic solution; section 3 describes the seismicity rate model. We describe the numerical methods in section 4 and the problem setup in section 5. We then present solutions for constant-rate injection (section 6) and finite duration injection (section 7) and discuss their implications. A model for the time dependence of earthquake magnitudes is presented in section 8.

2. Poroelastic Solution

The linear theory of poroelasticity was initially developed by Maurice Biot [*Biot*, 1941]. Other useful references include *Rice and Cleary* [1976], *Wang* [2000], and *Segall* [2010]. The constitutive equations for an isotropic, poroelastic medium relate the strains ϵ_{ij} linearly to the stresses σ_{ij} and changes in pore pressure p,

$$2\mu\epsilon_{ij} = \sigma_{ij} - \frac{\nu}{1+\nu}\sigma_{kk}\delta_{ij} + \frac{(1-2\nu)\alpha}{1+\nu}p\delta_{ij}, \tag{1}$$

where μ is shear modulus, ν is the drained Poisson's ratio (that is for no change in pore pressure), and α is the Biot coefficient. A second constitutive equation relates the change in pore fluid mass per unit volume of solid (measured in the unstrained state) to the volumetric strain and pore pressure

$$\Delta m = \alpha\rho_0\left[\epsilon_{kk} + \frac{\alpha p}{(\lambda_u - \lambda)}\right]. \tag{2}$$

Here ρ_0 is the fluid density (in the reference state), and λ, λ_u are the drained and undrained Lamé parameters. For undrained deformation $\Delta m = 0$. The Lamé parameters are related to Poisson's ratio via, $\lambda = 2\mu\nu/(1-2\nu)$

and $\lambda_u = 2\mu\nu_u/(1-2\nu_u)$. In this formulation of the isotropic Biot equations the four independent material parameters are μ, λ, λ_u, and α. (λ, λ_u can be replaced by ν and ν_u).

The stresses must satisfy the quasi-static equilibrium equations, which in the absence of body forces are $\sigma_{ij,j} = 0$. Conservation of pore fluid mass, combined with Darcy's law yields a diffusion equation in Δm

$$c\nabla^2 \Delta m = \frac{\partial \Delta m}{\partial t} + Q(\boldsymbol{x}, t), \tag{3}$$

where $Q(\boldsymbol{x}, t)$ is a fluid mass source and the hydraulic diffusivity c is a function of permeability k and fluid dynamic viscosity η

$$c = \frac{k}{\eta}\frac{(\lambda_u - \lambda)(\lambda + 2\mu)}{\alpha^2(\lambda_u + 2\mu)}. \tag{4}$$

Rudnicki [1986] gives the solution for a point source of fluid mass injection at time $t = 0$ and $r = 0$, where $r = ||\boldsymbol{x}||_2$. From this, superposition yields the pore pressure and stress for a specified injection history $q(t)$

$$p(\boldsymbol{x}, t) = \frac{1}{(4\pi)^{\frac{3}{2}}\rho_0 r^3}\frac{(\lambda_u - \lambda)(\lambda + 2\mu)}{\alpha^2(\lambda_u + 2\mu)}\int_0^t q(t')\xi^3 e^{-\frac{1}{4}\xi^2}\,\mathrm{d}t' \tag{5}$$

$$\sigma_{ij}(\boldsymbol{x}, t) = \frac{1}{2\pi\rho_0 r^3}\frac{\mu(\lambda_u - \lambda)}{\alpha(\lambda_u + 2\mu)}\int_0^t q(t')\left[\delta_{ij}(g - \xi g') + \frac{x_i x_j}{r^2}(\xi g' - 3g)\right]\mathrm{d}t', \tag{6}$$

where the similarity variable ξ is

$$\xi(t') = \frac{r}{\sqrt{c(t - t')}}. \tag{7}$$

The functions g and g' are defined as

$$g(\xi) = \mathrm{erf}\left(\frac{1}{2}\xi\right) - \frac{\xi}{\sqrt{\pi}}e^{-\frac{1}{4}\xi^2} \qquad g'(\xi) \equiv \frac{d}{d\xi}g(\xi) = \frac{1}{2\sqrt{\pi}}\xi^2 e^{-\frac{1}{4}\xi^2}. \tag{8}$$

For constant flux, $q(t) = q$, equations (5) and (6) can be integrated exactly [*Rudnicki*, 1986] yielding

$$p(\boldsymbol{x}, t) = \frac{q}{4\pi\rho_0 cr}\frac{(\lambda_u - \lambda)(\lambda + 2\mu)}{\alpha^2(\lambda_u + 2\mu)}\mathrm{erfc}\left(\frac{1}{2}\xi\right) = \frac{q}{4\pi\rho_0 r}\frac{\eta}{k}\mathrm{erfc}\left(\frac{1}{2}\xi\right), \tag{9}$$

$$\sigma_{ij}(\boldsymbol{x}, t) = -\frac{q(\lambda_u - \lambda)\mu}{4\pi\rho_0 cr\alpha(\lambda_u + 2\mu)}\left\{\delta_{ij}\left[\mathrm{erfc}\left(\frac{1}{2}\xi\right) - 2\xi^{-2}g(\xi)\right] + \frac{x_i x_j}{r^2}\left[\mathrm{erfc}\left(\frac{1}{2}\xi\right) + 6\xi^{-2}g(\xi)\right]\right\}. \tag{10}$$

Following integration over t', the variable ξ is now $\xi = r/\sqrt{ct}$. Note also that $q/\rho_0 c$ has units of length and the $1/r$ decay results from spherical spreading; this does not occur if diffusion is limited to two dimensions. The change in pore fluid mass is given by

$$\Delta m(\boldsymbol{x}, t) = \frac{q}{4\pi cr}\mathrm{erfc}\left(\frac{1}{2}\xi\right), \tag{11}$$

and is thus proportional to the pore pressure change.

It is worth noting that poroelastic coupling modifies the pore pressure change. From equation (2), pore pressure depends on both the change in fluid content, Δm, and volumetric strain, ϵ_{kk}. Furthermore, the hydraulic diffusivity differs depending on whether or not volumetric strain of the bulk solid is included in the storage coefficient (see discussion in *Wang* [2000]). In the computations that follow we refer to the *uncoupled* solution as one in which the solid stresses do not change; only the pore pressure changes due to injection. However, we include the coupling effects in the pore pressure distribution so that $p(\boldsymbol{x}, t)$ is exactly the same in both the coupled and uncoupled results. In this way any differences in seismicity rate between the coupled and uncoupled solutions are due solely to poroelastic changes in total stress.

3. Seismicity Rate

Dieterich [1994] developed a seismicity rate model that relates changes in Coulomb stress to changes in seismicity rate. The analysis considers a population of earthquake sources governed by rate and state friction that are accelerating toward instability, such that in the absence of stress perturbations the rate of earthquakes is constant in time.

We define the Coulomb stress $\tau = \tau_s + f(\sigma + p)$, where τ_s is the shear stress acting on a fault plane, σ is the normal stress (tension positive) acting on that plane, and f is the coefficient of friction. Define R as the rate of seismicity relative to the background rate, such that $R = 10^3$ corresponds to a thousandfold increase in the rate of earthquakes of a given magnitude. *Dieterich* [1994] derived a relationship for R in terms of a seismicity state variable; however, it is more convenient to eliminate this variable and write a single equation for R

$$\frac{\mathrm{d}R}{\mathrm{d}t} = \frac{R}{t_a}\left(\frac{\dot{\tau}}{\dot{\tau}_0} - R\right), \tag{12}$$

where $\dot{\tau}$ is the Coulomb stressing rate, $\dot{\tau}_0$ the background stressing rate, and $t_a \equiv a\bar{\sigma}/\dot{\tau}_0$ is a characteristic decay time. In the latter a is a constitutive parameter quantifying the direct effect on slip rate in the rate-state friction law, and $\bar{\sigma}$ is the background effective normal stress. Note from equation (12) that there is a steady state seismicity rate for a given stressing rate, $R_{ss} = \dot{\tau}/\dot{\tau}_0$. Thus, at steady state a tenfold increase in stressing rate yields a tenfold increase in seismicity rate.

When the stressing rate is far above background and seismicity has yet to increase, $\dot{\tau}/\dot{\tau}_0 \gg R$, and (12) integrates directly to

$$R \approx \exp(\Delta\tau/a\bar{\sigma}), \tag{13}$$

where $\Delta\tau$ is the change in Coulomb stress. This applies early in an injection sequence if the effective stressing rate is high relative to background stressing rate.

If, following a rapid increase in stress, the stressing rate returns to $\dot{\tau}_0$, the right-hand side of equation (12) is proportional to $R(1 - R)$. The resulting equation is separable, leading to

$$R = \frac{1}{(e^{-\Delta\tau/a\bar{\sigma}} - 1)e^{-t/t_a} + 1} \tag{14}$$

[*Dieterich*, 1994]. At $t = 0$ equation (14) reduces to (13), while for $t \gg t_a$ the seismicity rate returns to background, $R \to 1$. At short times $t/t_a < 1$ a Taylor series expansion of the exponential term gives

$$R \approx \frac{1}{e^{-\Delta\tau/a\bar{\sigma}} + t/t_a}, \tag{15}$$

which has the form of Omori's law [*Dieterich*, 1994], showing that we expect seismicity to decay proportional to t^{-1} following a rapid increase in stress.

There is no threshold stress in (12); an arbitrarily low stressing rate is hypothesized to cause a (possibly extremely) low background seismicity rate. It appears that (12) may be the simplest ordinary differential equation for seismicity rate that both admits a steady state solution and also predicts Omori-like decay following a rapid change in stress. A limitation of the *Dieterich* [1994] model is that it does not account for source-to-source stress interactions. Because the theory relates only to earthquake nucleations, it does not predict magnitude, although we return to this in section 8.

4. Numerical Method

The seismicity rate in equation (12) is driven by the Coulomb stressing rate $\dot{\tau} = \dot{\tau}_s + f(\dot{\sigma} + \dot{p})$. In the *uncoupled* limit, we set $\dot{\tau}_s = \dot{\sigma} = 0$, such that $\dot{\tau} = f\dot{p}$. For constant injection flux, we analytically differentiate equations (9) and (10) to obtain the stress and pore pressure rates as shown in Appendix A (equations (A7) and (A8)). In the more general case for time variable flux the stress and pore pressure rates are given in the form of integrals in Appendix A. The shear and normal traction rates $\dot{\tau}_s, \dot{\sigma}$ depend on the fault geometry and are computed from the unit fault normal and slip vectors.

We use ode45 in MATLAB to integrate the ordinary differential equation (12). The relative tolerance is 1e-6 and the absolute tolerance is set to a very small value so that error control is essentially only relative. For variable injection flux we compute the stress rate and pore pressure rate, in equations (A5) and (A6) using numerical quadrature.

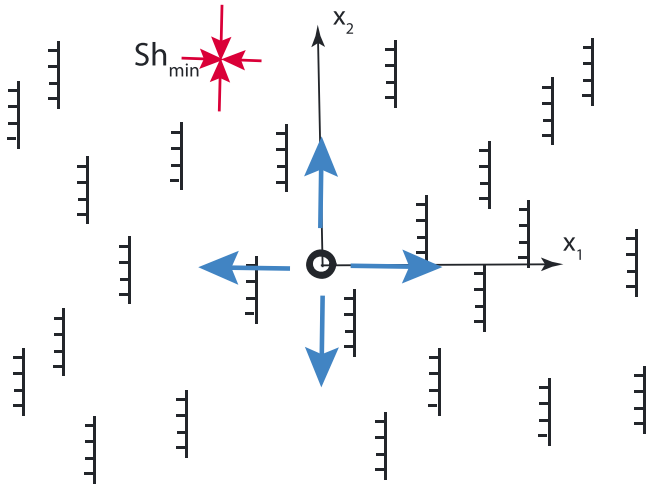

Figure 2. Map view of fault geometry relative to the injector. Normal faults dip to the west (left). Corresponding horizontal stress state is shown, with least principal horizontal compressive stress normal to the strike of the faults.

5. Problem Setup

We consider a specified injection rate at a point ($r = 0$) in a homogeneous full space. To compute shear and normal tractions, one must specify the orientation of the faults and the slip direction on those faults. In the examples here we choose the faults to be N-S striking normal faults, dipping 60° to the west as in Figure 2. The unit normal to the faults is $\hat{\boldsymbol{n}} = [-0.866, 0, 0.5]^T$, while the unit slip vector is $\hat{\boldsymbol{s}} = [-0.5, 0, -0.866]^T$. The faults are uniformly distributed throughout the medium; the elastic and hydraulic properties of the faults are the same as the background medium. Implicit in this picture is a stress state in which the least horizontal normal stress strikes E-W, although only stress rates enter equation (12).

The nominal material parameters used in the calculations are given in Table 1. For Berea sandstone *Hart and Wang* [1995] report an average for five samples of the Skempton's coefficient, $B = 0.75$. The Biot coefficient α is then computed via

$$\alpha = \frac{3(\nu_u - \nu)}{B(1 + \nu_u)(1 - 2\nu)}, \tag{16}$$

Table 1. Nominal Parameters Used in This Work

Parameter	Variable	Value and Unit
	Poroelastic Properties	
Shear modulus	μ	20 GPa
Drained Poisson's ratio	ν	0.25
Undrained Poisson's ratio	ν_u	0.3
Skempton's coefficient	B	0.75
Biot coefficient	α	0.31
	Transport Properties	
Permeability	k	3×10^{-16} m^2
Fluid Viscosity	η	0.4×10^{-3} Pa s
Hydraulic diffusivity	c	6.8×10^{-2} m^2/s
Reference fluid Density	ρ_0	10^3 kg/m^3
Volume injection rate	q/ρ_0	0.01 m^3/s
	Friction Properties and Stress State	
Direct velocity strengthening magnitude	a	0.003
Nominal friction	f	0.6
Effective normal stress	$\bar{\sigma}$	16.67 MPa
Background stressing rate	$\dot{\tau}_0$	0.001 MPa/yr

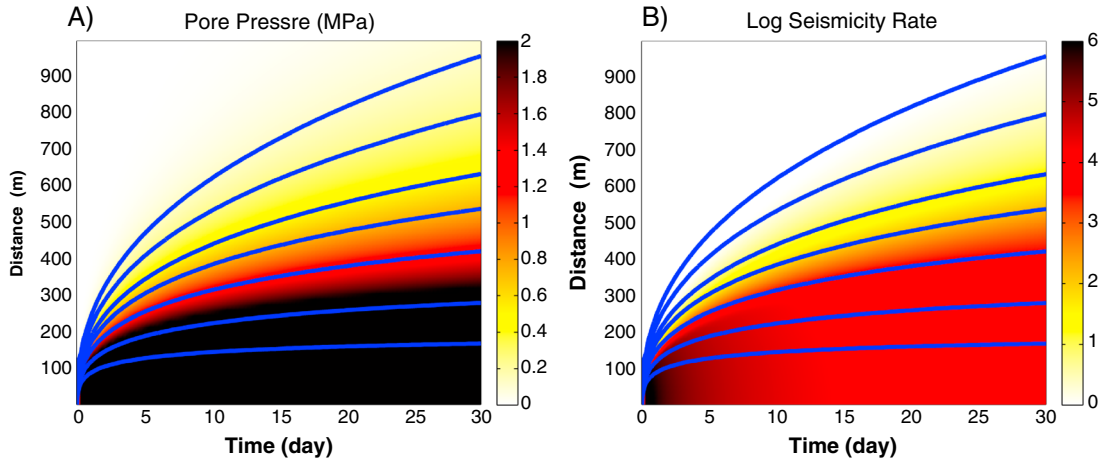

Figure 3. Results for constant injection rate. (a) pore pressure $p(x_1, t)$ as a function of space and time. Contours at 0.125, 0.25, 0.5, 0.75, 1.25, 2.5, and 5.0 MPa. (b) Corresponding seismicity rate, $\log_{10} R(x_1, t)$. x_1 is the E-W direction perpendicular to fault strike. Contours in Figure 3b show constant p as in part (Figure 3a).

[*Segall*, 2010, equation (10.15)]. Volume injection rates range from roughly 350 m^3/d in Youngstown [*Kim*, 2013], to about 1000 m^3/d in the Paradox Basin [*Ake et al.*, 2005]. For calculations here we use an injection rate of 900 m^3/d. The fluid viscosity is estimated as that for pure water at 350°K. We take a permeability of 3×10^{-16} m^2 which leads to a hydraulic diffusivity of $c \sim 0.07$ m^2/s, from equation (4). This combination of parameters yields a length scale of $q/\rho_0 c = 0.15$ m.

For friction parameters we assume a nominal friction coefficient of 0.6, and the direct effect parameter $a = 0.003$ [*Marone*, 1998]. The background effective normal stress $\bar{\sigma}$ is taken to be appropriate for lithostatic minus hydrostatic pore pressure at a depth of 1 km for a rock density of 2700 kg/m^3. The background stressing rate is assumed to be appropriate for a stress drop of 1 MPa every 1000 years. This leads to a characteristic time $t_a = a\bar{\sigma}/\dot{\tau}_0$ of roughly 50 years. We vary this parameter to test its significance on the predicted seismicity rate.

6. Constant Injection Rate

Figure 3a shows the pore pressure distribution in space and time $p(x_1, t)$ for the base case parameters and constant injection rate (x_1 is along the east direction in Figure 2). As expected, the $1/r$ behavior causes p to decay rapidly with distance from the injector. Figure 3b shows the corresponding seismicity rate on a logarithmic scale, $\log_{10} R$. The contours in Figure 3b denote equal pore pressure change, as in Figure 3a. This highlights that the onset of seismicity nearly follows a space-time trajectory of the perturbation in pore pressure, as assumed in work of, for example, *Shapiro et al.* [1997, 2002], shown in Figure 1 here.

The seismicity rate eventually peaks and then slowly declines, as is apparent closer to the injector in Figure 3b. This occurs, according to equation (12), as the seismicity rate approaches steady state, and R tracks the decreasing Coulomb stressing rate. A decrease in seismicity rate near the injection point has been observed in some field cases, for example the 1993 Soultz-sous-Forêts injection experiment (Figure 1).

Figure 4 shows the seismicity rate for the same parameters, but ignoring poroelastic coupling. As discussed in section 2, the pore pressure fields are specified to be the same in both coupled and uncoupled solutions, so that the difference is solely due to coupling-induced changes in stress. Comparing Figures 4a and 3b, it is apparent that at a given time elevated seismicity extends a greater distance from the injector in the uncoupled case. Figure 4b shows the normalized difference $\log_{10}[(R_u - R)/R]$, where R_u is the relative seismicity rate ignoring coupling-induced stress changes. The uncoupled solution overestimates the seismicity rate, particularly at distances (times) just beyond (before) substantial increases in pore pressure, where the difference can be a factor of 100 or more. Whether coupling-induced stresses increase or decrease seismicity depends on the geometry of the faults relative to the injector, as discussed below.

The effect of poroelastic coupling on the seismicity rate is understood, as follows: Increased pore pressure near the injector causes the rock to expand volumetrically. This expansion leads to radially outward displacements which decrease with distance from the injector. Thus, the radial strain, and thus stress, are compressive. Along the x_1 direction horizontal compression increases fault normal compression for NS striking normal faults. The

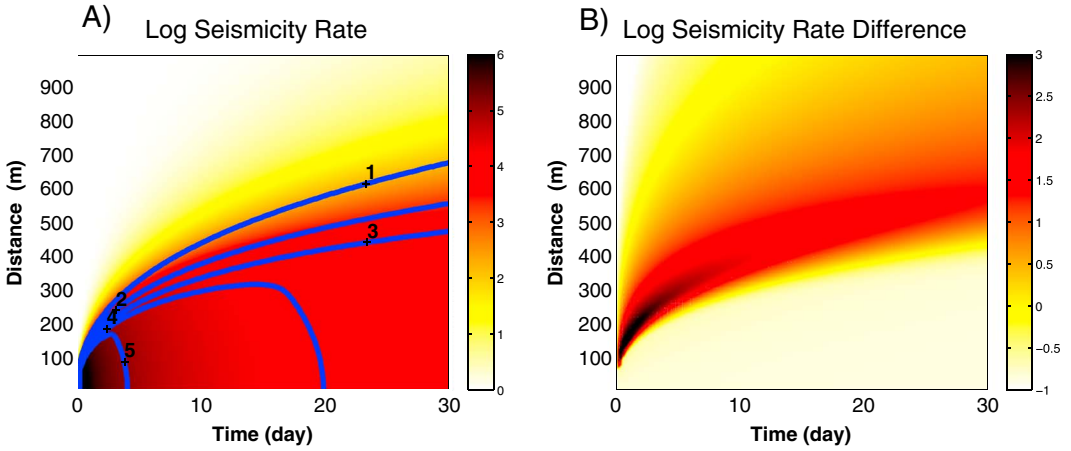

Figure 4. Effect of poroelastic coupling for steady injection. (a) $\log_{10} R$ for base case parameters, as in Figure 3b but ignoring coupling-induced stress changes. Contours show the seismicity rate change including coupling, to facilitate the comparison. (b) Relative difference between uncoupled and coupled solutions $\log_{10}[(R_u - R)/R]$.

shear traction on the faults also decreases, both effects decrease the Coulomb stress. The uncoupled solution ignores this effect and thus overpredicts the seismicity rate ahead of the large pore pressure changes. Closer to the injector the effect of coupling is rather small, and the coupled and uncoupled solutions predict similar seismicity rates.

The spatial dependence of the poroelastic stresses relative to the direct pore pressure effect is illustrated in Figure 5. Near the injector, the pore pressure change is dominant, whereas at greater distance the poroelastic stresses dominate. This can be understood by considering the stresses induced if there were a permeability barrier at some distance from the injector. Pore pressure increases would be limited to the volume inside the barrier; however, the volumetric expansion inside that region would generate elastic stresses that extend well outside that region. This is consistent with the conclusion of *Rozhko* [2010] that solid stresses extend beyond the larger pore pressure changes.

Because poroelastic expansion induces a radially compressive stress the induced seismicity rate change differs along the x_1 and x_2 axes. Along the x_2 direction the radial stress does not induce tractions acting on NS striking fault planes (in the $x_3 = 0$ plane). (However, the hoop stress $\sigma_{\theta\theta}$, is extensional and does induce tractions along the x_2 direction). The orientation of the faults breaks the symmetry of the problem, such that even though

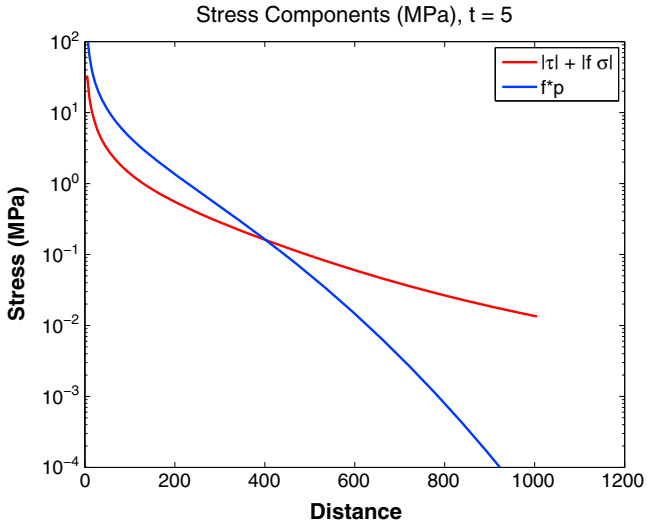

Figure 5. Poroelastic stress compared to direct pore pressure effect as a function of distance (x_1 axis) at $t = 5$ days. Sum of absolute values of shear (τ_s) and normal stress contributions ($f\sigma$) to Coulomb stress are shown for 60° dipping normal faults.

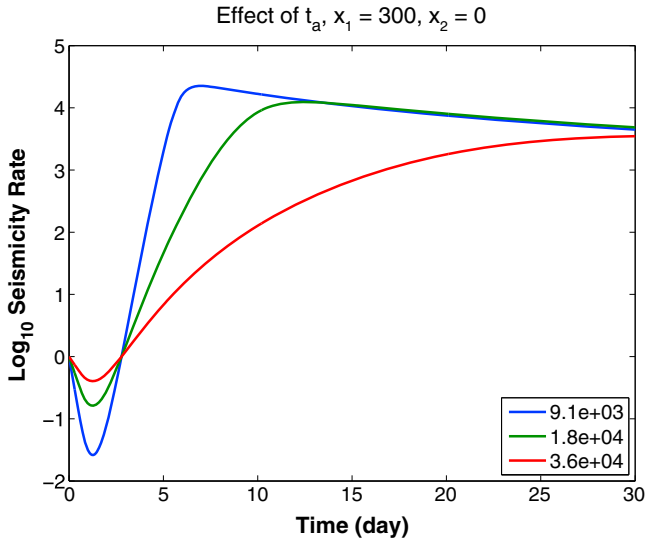

Figure 6. Log seismicity rate at $x_2 = 0, x_1 = 300$ m for different t_a, where t_a is in days.

the material properties are spatially uniform and isotropic, the seismicity response is not radially symmetric. We illustrate this in more detail below for finite duration injection.

The predicted seismicity rate depends both on the perturbing pore pressure and stresses, as well as the characteristic decay time t_a. Figure 6 shows $\log_{10} R$ at $x_2 = x_3 = 0, x_1 = 300$ m for the standard parameters as well as for a factor of 2 increase and decrease in t_a (t_a was altered by changing $a\bar{\sigma}$). Smaller t_a leads to faster changes in seismicity rate as well as a larger peak earthquake rate. The early decrease in seismicity rate results from poroelastic stresses, which act to decrease the Coulomb stress on NS striking normal faults at this location, as discussed above. At $x_1 = 300$ m the characteristic diffusion time is $x_1^2/4c \sim 3.8$ days. Prior to this the compressive stressing ahead of the diffusion front dominates the Coulomb stress change leading to a decrease in seismicity rate. If the background rate of earthquakes is already low, this decrease is unlikely to be observed. For times greater than $x_1^2/4c$ the Coulomb stress change is dominated by the increase in pore pressure. At some time, depending on t_a the seismicity rate reaches steady state and gradually declines as the Coulomb stressing rate declines.

6.1. Short-Time Approximation

At short times following the onset of injection, the seismicity rate, from equation (13) is $R \approx exp(\Delta\tau/a\bar{\sigma})$. Ignoring poroelastic stressing and assuming that the Coulomb stress change is driven solely by changes in pore pressure,

$$R(\boldsymbol{x}, t) \approx \exp[fp(\boldsymbol{x}, t)/a\bar{\sigma}]. \tag{17}$$

As detailed in Appendix B, this allows us to approximate the space-time relationship for the point at which the seismicity rate reaches some critical rate R_c (for example, the rate at which seismicity would clearly be detectable over the background rate),

$$r \approx \sqrt{f_c(r, R_c)ct},$$

where

$$f_c(r, R_c) \equiv \left\{ 2\mathrm{erfc}^{-1}\left[\frac{a\bar{\sigma}}{f\Lambda}\frac{4\pi r}{r_q}\log(R_c)\right]\right\}^2$$
$$\Lambda \equiv \frac{(\lambda_u - \lambda)(\lambda + 2\mu)}{\alpha^2(\lambda_u + 2\mu)}$$
$$r_q \equiv q/\rho_0 c \tag{18}$$

and erfc^{-1} is the inverse of the complementary error function, Λ is a combination of moduli with units of stress, and r_q is a characteristic length scale. The time to reach a critical seismicity rate scales with r^2/c, where c is modified by the parameter f_c that depends on both distance as well as poroelastic and frictional parameters.

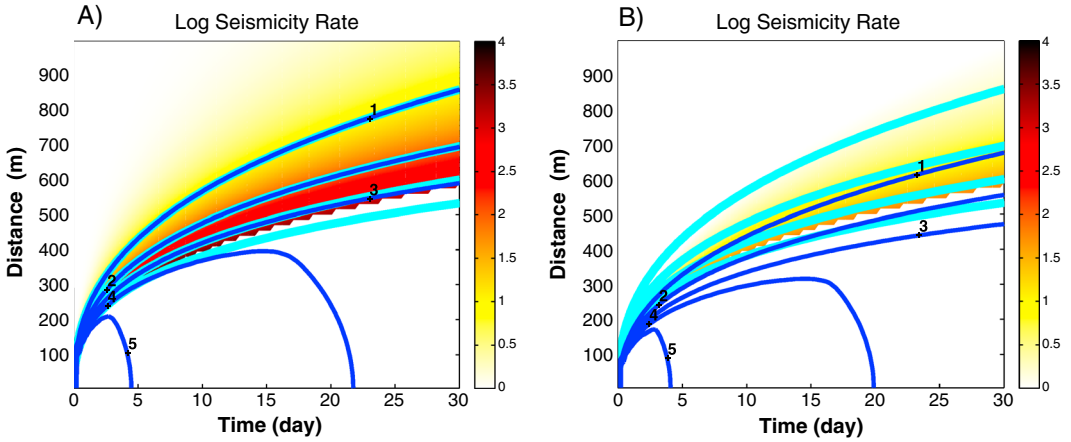

Figure 7. Accuracy in the short-time approximation to seismicity rate, given by equation (17). (a) Uncoupled and (b) coupled. Color scale and dark blue contours illustrate $\log_{10} R$. The seismicity rate is only colored in the range $t < t_s(r)$, where the approximation is valid according to equation (19). The cyan contours $\log_{10} R = 1, 2, 3, 4$ show the approximate seismicity rate, given by equation (18).

Equation (17) is a "short-time" approximation, since it applies only at times when $R \ll \dot{\tau}/\dot{\tau}_0$. The approximation is expected to break down when $\dot{\tau}/\dot{\tau}_0 \sim R$. The domain $t < t_s$ where the short-time approximation should be valid is found in Appendix B to be

$$t_s \approx \frac{r^2}{c f_s(r)}$$
$$f_s(r) \equiv \left\{ 2\mathrm{erfc}^{-1}\left[\frac{a\bar{\sigma}}{f\Lambda} \frac{4\pi r}{r_q} \log\left(\frac{\Lambda}{\dot{\tau}_0} \frac{q/\rho_0}{8\pi^{\frac{3}{2}} r^3} \right) \right] \right\}^2 . \quad (19)$$

Figure 7 compares the short-time approximation, equation (17) with the full numerical solution. The color scale for $\log_{10} R$ is shown only for $t < t_s(r)$. Figure 7a shows the response ignoring poroelastic coupling, whereas Figure 7b includes coupling-induced stress changes. Considering Figure 7a, we see that for the parameters chosen, the short-time approximation is quite accurate in predicting seismicity rate changes for $t < t_s(r)$. For $t > t_s(r)$ the approximation begins to break down, as suspected. For example, the contour for $R = 10^4$ is valid only for times less than $\sim$ 10 days.

The approximation in (17) assumes that the seismicity is driven solely by changes in pore pressure. Figure 7b compares the approximation with the numerical results including poroelastic stressing. In this case the approximation over predicts the seismicity rate by a factor of 10 or more, even for $t < t_s$. This is due to the neglect of coupling-induced stress changes, as is made clear by the difference in seismicity rate between the coupled and uncoupled numerical solutions (Figure 4b). Interestingly, the shape of the approximate and numerical contours for the onset of seismicity is roughly the same, reflecting the dominant effect of diffusion on the seismicity rate.

It has been common to fit curves of the form $t = r^2/c$ to the onset of seismicity [e.g., *Shapiro et al.*, 1997, 2002], and Figure 1 here. In some cases this has been used to infer the average hydraulic diffusivity of the seismically active volume. Equation (18) shows that $t = r^2/c$ does approximate the onset of seismicity at a given level as long as coupling-induced stresses are negligible. However, even in this limit the apparent diffusivity is modified by a factor of $f_c(r, R_c)$, that also depends on frictional and poroelastic properties. $f_c(r, R_c)$ is illustrated in Figure 8 for $R_c = 10^3$ and 10^4 and nominal properties and ranges from near 1 to more than 10. For moderate distance $f_c(r, R_c)$ is greater than one, suggesting that fitting $t = r^2/c$ curves to seismicity onset may bias the inferred diffusivity to higher values.

7. Finite Duration Injection

We next consider constant-rate injection q over the finite time interval $0 < t < T$. Given that the poroelastic equations are linear, this is simply achieved by superimposing the solution for flux q starting at $t = 0$ with the solution for flux $-q$ beginning at $t = T$. The stress and pore pressure rates are then used to compute the

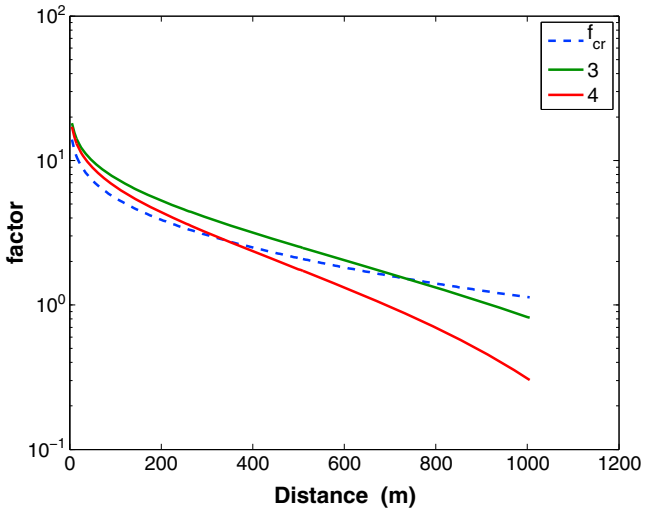

Figure 8. Factors that modify the inferred diffusivity. $f_c(r, R_c)$ from equation (18) is shown for $R_c = 10^3$ and 10^4 as solid curves. $f_s(r)$ from equation (19) is shown with dashed curve.

seismicity rate according to (12). Figure 9 shows the seismicity rate along both the x_1 and x_2 axes for injection at constant rate for $T = 15$ days. As discussed previously, seismicity along the x_1 direction is suppressed by poroelastic stressing, both in an absolute sense and relative to seismicity along the x_2 direction.

Following shut-in the seismicity rate near the injector plummets as the pore pressure drops. In the far field the seismicity rate continues to increase due to diffusion in both x_1 and x_2 directions. Surprisingly, at intermediate distances along the x_1 axis the seismicity rate rapidly increases following shut-in. This is due to the release of poroelastic stress and is not observed along the x_2 axis. The mechanism can be understood by examining the poroelastic stress changes as in Figure 10. During injection both the shear and normal stress decrease (negative normal stress is compression), causing the Coulomb stress change to be less than *fp*. Following shut-in the fault normal compression rapidly decreases, and the shear stress increases; both effects contribute to an increase in Coulomb stress. Thus, at the same time the fault is positively stressed the pore pressure continues to increase, leading to a rapid increase in Coulomb stress. This causes the post shut-in spike in seismicity rate. Note from Figure 10 the rapid stress change while pore pressure is still increasing is independent of the *Dieterich* [1994] model for seismicity rate.

Figure 11 shows the evolution of seismicity in the x_1, x_2 plane following shut-in, with seismicity rate on a linear scale. At shut-in (Figure 11a) seismicity is slightly elongate in the along-strike, x_2, direction due to poroelastic

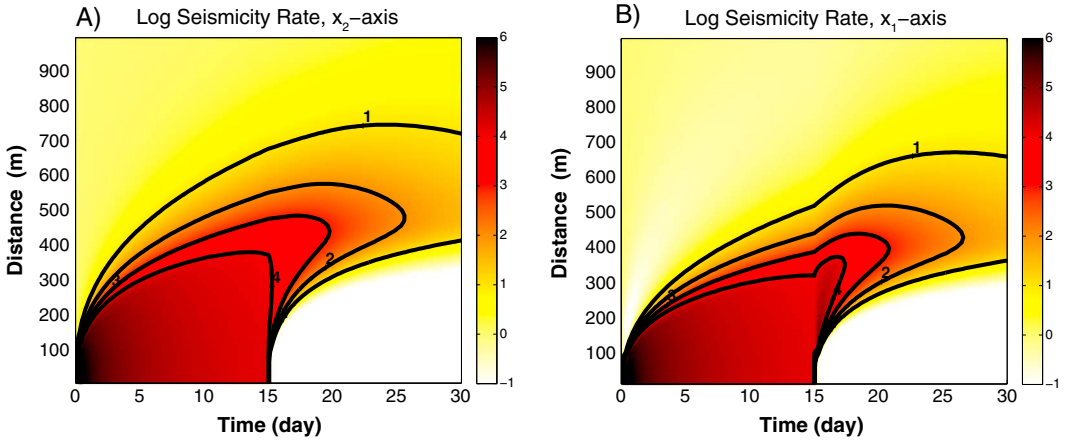

Figure 9. Space-time plot of seismicity rate for constant flux injection for 15 days. (a) Distance along x_2 axis; (b) distance along x_1 axis. Color scale and contours represent $\log_{10}$ of seismicity rate.

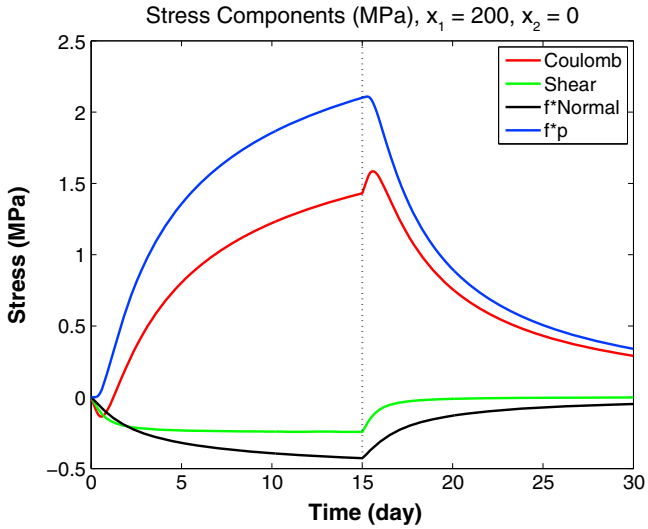

Figure 10. Stress changes during finite duration injection at constant rate, at a point ($x_1 = 200, x_2 = 0$) m. The stress components which sum to the Coulomb stress change are shear stress, τ_s, normal stress $f\sigma$, and pore pressure fp. Dotted vertical line indicates the shut-in time.

stressing. Shortly after shut-in (Figures 11b–11d) the seismicity rate peaks at azimuths in the x_1 direction and diffuses away from the injector with decreasing amplitude.

Figure 12 illustrates how t_a influences the amplitude and duration of the post shut-in peak in seismicity rate for factor of 2 changes in t_a. For the nominal t_a the local seismicity rate jumps by a factor of more than three at this particular location following shut-in. For the smaller t_a the increase is closer to a factor of 6. Note that for both $t_a = 9.1 \times 10^3$ days and $t_a = 1.8 \times 10^4$ days the seismicity is declining and reaches steady state (i.e., is independent of t_a) prior to shut-in. For the longest t_a the seismicity steadily increases prior to shut-in. In all three cases the highest rate occurs in the postinjection period. Recall that the rate increase occurs only in some locations (Figure 11) depending on the geometry of the faults relative to the injector.

The post shut-in spike in seismicity results from the rapid change in stress, before the pore pressure has had a chance to decline. This suggests that slowly tapering the injection would slowly restress the faults, allowing time for the pore pressure to decrease by diffusion. We explore this by applying a Gaussian taper to the injection rate after 15 days of constant-rate injection. In this numerical test (Figure 13), we apply tapers of duration 2 and 5 days. For these parameters, a taper of 5 days nearly completely eliminates the localized increase in seismicity (Figure 13). These calculations are for the nominal characteristic decay time t_a; the particular response will of course depend on both t_a and the duration of the taper, as well as location.

8. Magnitude Dependence

The *Dieterich* [1994] model approximates the rate of earthquake nucleations but says nothing about the resulting magnitudes. A rigorous analysis of triggered earthquake magnitudes would need to specify the spatial distribution of frictional properties, fault geometry, and background stress state, in order to predict how far a dynamic rupture would propagate before arresting. This is clearly beyond the scope of the simplified analysis developed here. However, we propose that useful progress can be made by considering that the rate of occurrence of magnitude M earthquakes depends on (1) the rate of nucleations, (2) the size distribution of fault segments or patches that can rupture during a single event, and (3) the stress distribution necessary to sustain rupture once initiated.

For induced seismicity the third term warrants particular consideration. A number of numerical studies of dynamic ruptures on flat faults with strong frictional weakening at high slip speeds, due either to thermal pressurization and/or flash heating [e.g., *Rice*, 2006], show that self-sustaining ruptures are possible at quite low background ratios of shear to normal stress, on the order of $\sim$ 0.15 to 0.2 [*Noda et al.*, 2009; S. V. Schmitt et al., Nucleation and dynamic rupture on weakly stressed faults sustained by thermal pressurization, submitted to *Journal of Geophysical Research*, 2015]. However, if the background shear to normal stress ratio is

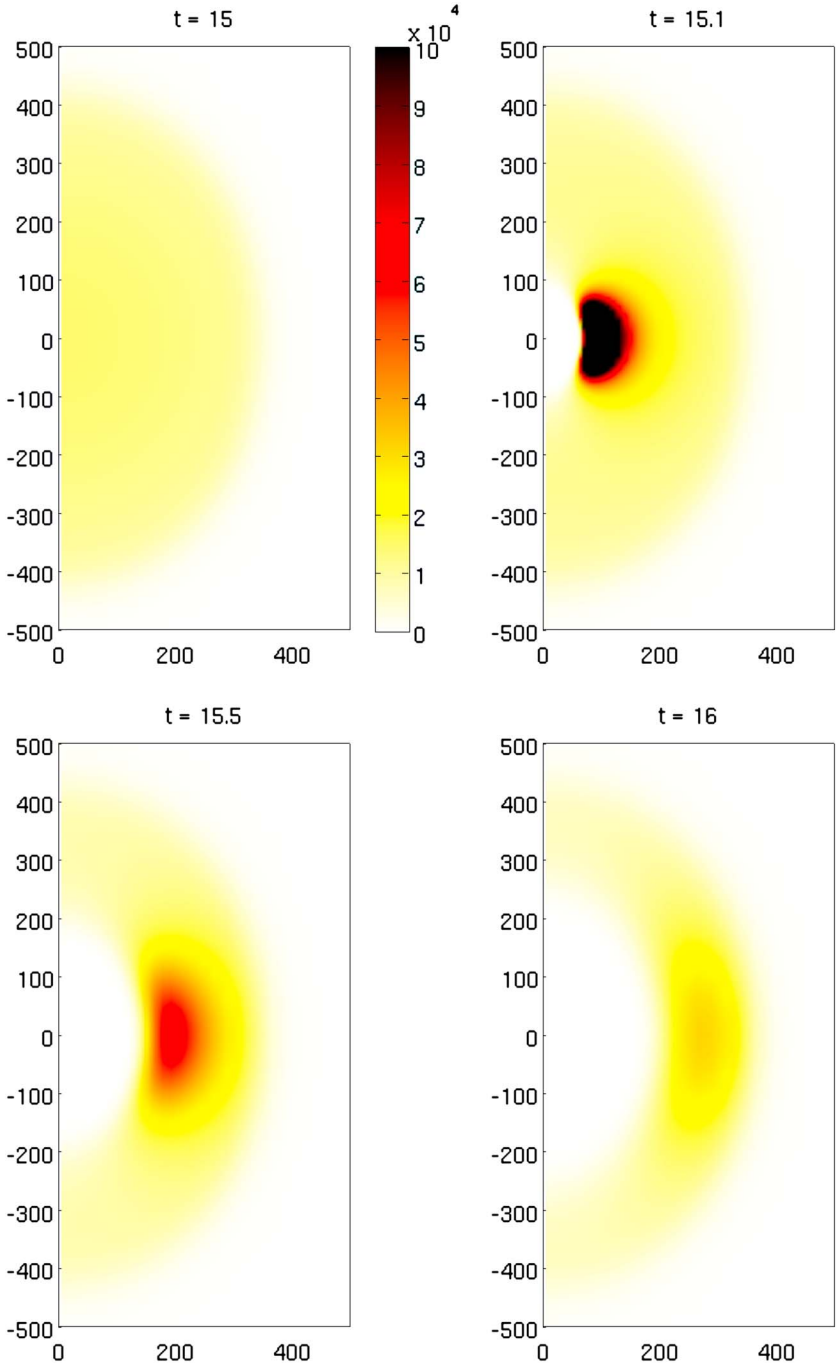

Figure 11. Space-time evolution of seismicity rate following shut-in (linear scale). Each panel shows $R(x_1, x_2)$ at (a) shut-in, $t = 15$ days, (b) $t = 15.1$ days, (c) $t = 15.5$ days, and (d) $t = 16$ days.

less than this threshold, ruptures that initiate at stress (or strength) heterogeneities arrest after propagating a relatively short distance (S. V. Schmitt et al., submitted manuscript, 2015).

Based on these considerations, we propose that the rate of magnitude M events can be computed as the product of three factors. The first is the rate of nucleations, R. The second is the probability that the nucleation occurs on a fault segment with size sufficient to yield a magnitude M event given a typical static stress drop. Denote this probability $P\left(r_s(M)\right)$, where $r_s(M)$ is the source radius of a magnitude M event. These two factors alone would be sufficient for a relatively high shear stress environment in which a rupture, once nucleated, can propagate over the full fault segment. If on the other hand the background shear stress is too low, an

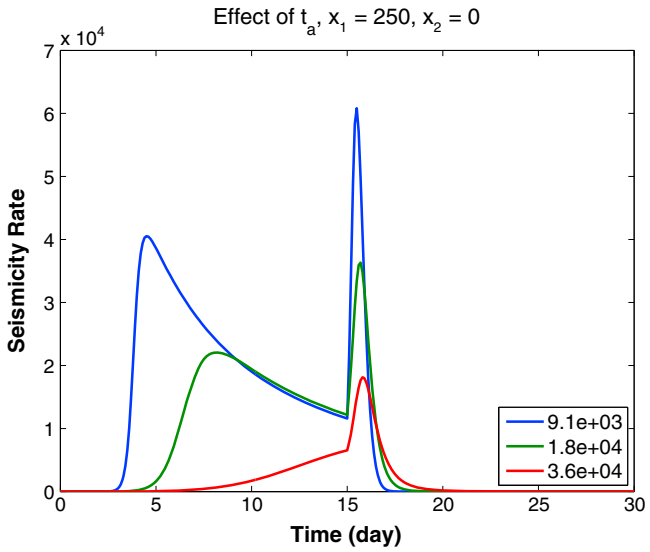

Figure 12. Effect of t_a on post shut-in peak in seismicity rate, at $x_1 = 250$ m, $x_2 = 0$ for three different values of t_a (in days).

artificially nucleated earthquake will arrest before rupturing the full segment. It is likely that the ambient shear stress in many fluid injection environments is too low to sustain rupture over parts of a fault segment on which the Coulomb stress is not perturbed by injection. This is clearly an end-member case, the other (high-stress) end-member being one in which a rupture once nucleated can propagate over the full segment. We need not distinguish whether the segment boundaries are defined by fault geometry or spatial distribution of prestress, including the stress from previous earthquakes. Our approach for the low ambient shear stress limit follows that of *Shapiro et al.* [2013], who suggested that source segments must lie fully within the region perturbed by injection.

In Appendix C we derive the probability that a circular crack of radius r_s with some point within a unit sphere lies completely within that sphere, we denote this P_{in}. The dependence of P_{in} on r_s is shown in Figure 14.

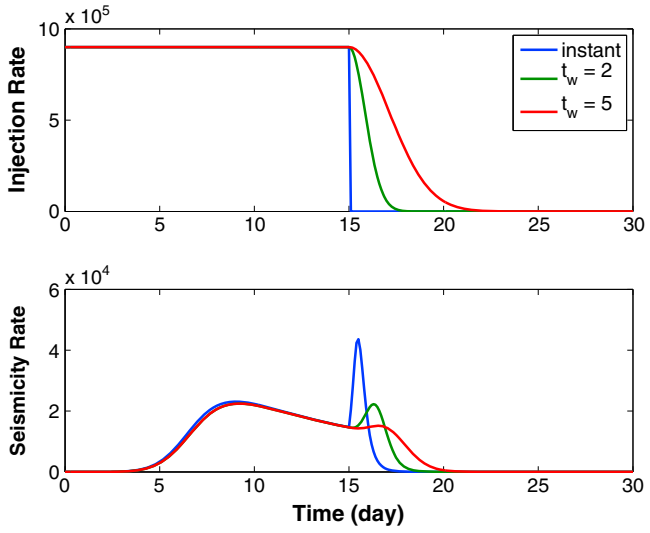

Figure 13. Effect of Gaussian taper on seismicity rate. (a) Injection rate $q(t)$, either instantaneous, or with Gaussian taper with taper width of 2, 5 days. (b) Corresponding seismicity rate. Nominal t_a.

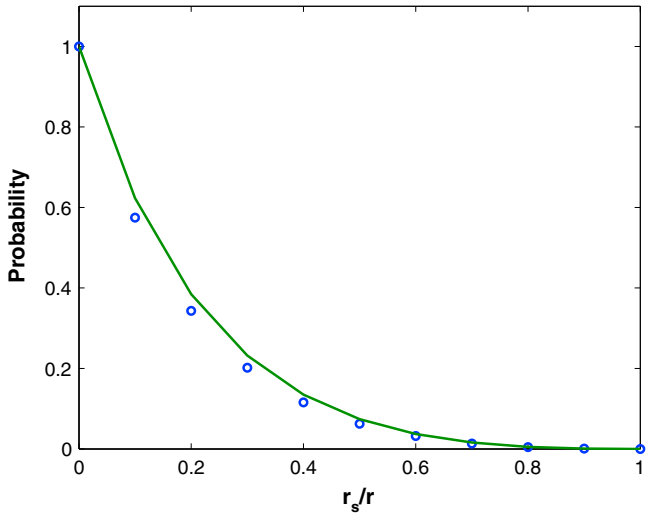

Figure 14. Probability that a crack of radius r_s that is at least partly in a sphere of radius r is completely within that sphere. Solid line from equation (C2), circles are random simulations.

Given that the radius of the perturbed zone grows with $\sqrt{4ct}$, the total rate of magnitude M events in a low shear stress environment is,

$$R(M,t) = \int R(\boldsymbol{x},t)\, P\left(r_s(M)\right) P_{\text{in}}\left(\frac{r_s(M)}{\sqrt{4ct}}\right) \mathrm{d}V. \tag{20}$$

The first term is the rate of nucleations, the second the probability that the nucleation occurs on a "magnitude M segment," while the third is the probability the segment lies entirely within the perturbed zone. For simplicity we assume P_{in} does not depend on position $\boldsymbol{x}$, that is the probability is the same regardless of where the nucleation occurs. If we further assume that the sources are randomly distributed in space, with size distribution appropriate to generate background seismicity (in the absence of injection-induced perturbation) with Gutenberg-Richter distribution then $P\left(r_s(M)\right)$ follows a Gutenberg-Richter distribution. In this case equation (20) becomes

$$R(M,t) = k10^{-bM} P_{\text{in}}\left(\frac{r_s(M)}{\sqrt{4ct}}\right) \int R(\boldsymbol{x},t)\mathrm{d}V \tag{21}$$

where the constant k accounts for the background rate of $M = 0$ events (at background stressing $R = 1$ and $P_{\text{in}} = 1$ such that $R_0 = k\int dV$). Note that the time dependence of magnitude M events comes from both the time-dependent nucleation rate and the time-dependent radius of the perturbed volume, which we have assumed scales with the diffusion distance $\sqrt{4ct}$.

Equation (21) is used to simulate $R(M,t)$ for a range of magnitudes in Figure 15. The source radii are computed using standard earthquake scaling relations assuming a stress drop of 3 MPa. Only the relative seismicity rates are meaningful since R is scaled by the background seismicity rate. The maximum magnitude is controlled by the radius of the perturbed zone $\sqrt{4ct_{\text{max}}}$ where t_{max} is 30 days. Figure 15 shows that, given some detection threshold, we predict a finite period with no observable seismicity. The duration of the quiescent period increases with magnitude. For this particular fault geometry there is a barely noticeable increase in seismicity rate following shut-in, even though the rates in Figure 15 integrate over the full model domain (Figure 12 shows seismicity at a particular location). Following the peak in seismicity the rate declines with time in a way that depends both on pore pressure diffusion and t_a. *Bachmann et al.* [2011] show that postinjection seismicity at Basel decays following Omori's law.

Figure 16 illustrates the frequency-magnitude relationship at different times as injection proceeds, assuming that the intrinsic b value is 1.0. At early times the distribution is depleted in larger events, but as time increases this "roll over" occurs at progressively larger magnitudes. At intermediate magnitudes the apparent b value is greater than 1.0 consistent with numerous observations of induced earthquakes. For example, *Dorbath et al.* [2009] show a roll off for Soultz-sous-Forêts injections in 2000 and 2003 at about the magnitude 2.0 to 2.3 range. *Eaton et al.* [2014] suggests that b values greater than 1 reflect inherent length scales introduced by

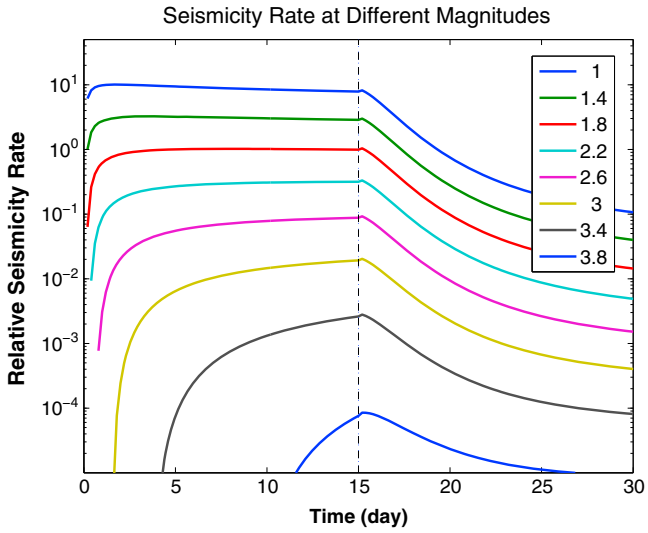

Figure 15. Seismicity rate $R(M)$ averaged over the full computational domain, on log scale, as a function of time for different magnitudes. Only the relative rates are significant. Magnitudes are computed based on standard scaling laws and a 3 MPa stress drop. Vertical line indicates cessation of injection.

stratigraphic layering, although the departure from the Gutenberg-Richter distribution at high magnitude is observed in granites at Soultz [*Dorbath et al.*, 2009], demonstrating that layering is not required.

Figure 17 shows a simulation of event magnitudes as a function of time, based on the seismicity rates shown in Figure 15. Random event times are chosen with the number of earthquakes at each magnitude level proportional to $R(M,t)$. We first compute the total number of earthquakes in each time interval of length Δt as $N(t) = \Delta t \int_{M_{\min}}^{M_{\max}} R(M,t)\mathrm{d}M$, where $M_{\min}$ and $M_{\max}$ are the minimum and maximum magnitude, and we approximate the integral over time simply as $R\Delta t$. In the low shear stress environment $M_{\max}$ is constrained by the volume of the perturbed zone at the final time. Next, define the cumulative distribution function of magnitude (at fixed time) as

$$F(M;t) \equiv 1 - \frac{\int_{M}^{M_{\max}} R(M,t)\mathrm{d}M}{\int_{M_{\min}}^{M_{\max}} R(M,t)\mathrm{d}M}. \tag{22}$$

The magnitudes of the $N(t)$ events at time t are determined from the inverse distribution function $M = F^{-1}(\chi)$, where χ is a random vector of length $N(t)$ with elements in the interval $[0, 1]$.

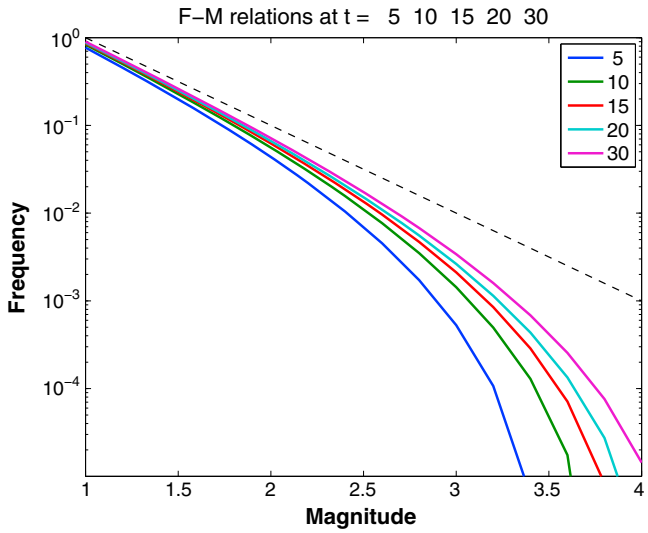

Figure 16. Frequency-magnitude relations at different times (in days). Dashed line indicates slope of −1.

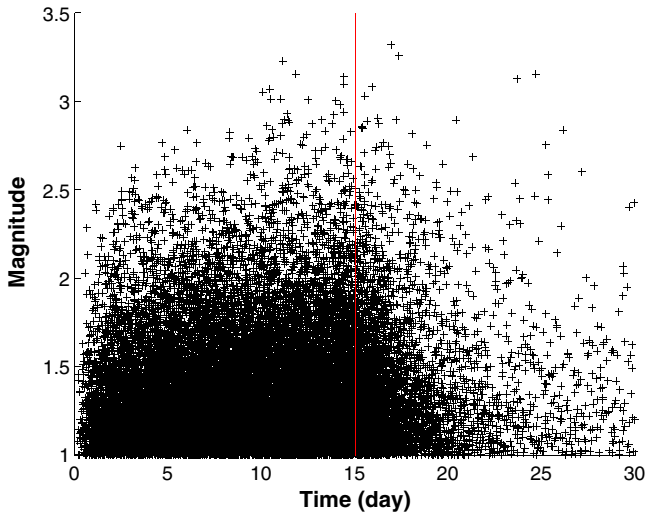

Figure 17. Simulation of earthquake magnitudes at different times based on the seismicity rates shown in Figure 15. Vertical line indicates cessation of injection.

In Figure 17 the maximum magnitudes increase with time as the perturbed volume increases. If the overall seismicity rate is sufficiently high, it is not atypical for the largest events to occur post shut-in, as in Figure 17. (*Baisch et al.* [2010] also show an increase in simulated event magnitude with time due to pore pressure diffusion in a model fault consisting of coupled spring slider blocks.) At later times the maximum magnitudes decrease, as the seismicity rate decreases at all magnitudes, consistent with the seismicity rate curves in Figure 15.

Additional work will be required to understand how the behavior changes for different injection scenarios, material properties and stressing rates. We have emphasized the low shear stress limit where the maximum magnitude of an event is, in part, controlled by the volume of the zone perturbed by injection. If the background shear to normal stress ratio is sufficiently high, it is possible an event once nucleated will extend well beyond the perturbed region. In this case the maximum magnitude is constrained only by the size of the faults present and the distribution of tectonic stress on those faults.

9. Discussion

We have explored a rather idealized case with a uniform distribution of faults, such that the probability of nucleating an event at a particular point in space depends only on the pore pressure and stress, rather than the distribution of preexisting faults. In the likely event that faults are nonuniformly distributed the details of the predicted behavior could be quite different. For example, if faults are concentrated in a direction where shut-in-induced stresses are stabilizing, then we would not anticipate an increase in seismicity rate following shut-in. If on the other hand, faults are concentrated in locations where shut-in is destabilizing, then a more pronounced increase in seismicity following shut-in would be expected. We also only considered a single fault orientation. One could extend the analysis to include multiple fault orientations allowing nucleation on faults that are critically stressed by the sum of the background tectonic stress and the perturbing injection-related stresses.

Faults are also possibly highly conductive pathways that could strongly influence the pore pressure distribution. In addition, many waste water injection wells are drilled into layered sedimentary sequences in which permeability varies strongly between layers. These effects have been the subject of previous studies [e.g., *Zhang et al.*, 2013]; we have chosen here to focus on the simple, homogeneous case to highlight the first-order effects of poroelastic coupling and rate-dependent earthquake nucleation. Additional studies will be needed to explore the consequences of poroelastic coupling with heterogeneous hydraulic properties.

The *Dieterich* [1994] model relating stress to seismicity rate changes is certainly oversimplified. One assumption is that the background stress is sufficiently high relative to the shear resistance that the background stressing rate leads to a nonzero (although potentially exceedingly small) background seismicity rate. The model would require modification to include a (pressure-dependent) threshold stress below which the seismicity rate vanishes. Given some distribution of preexisting faults, it would be reasonable to anticipate that the threshold strength varies spatially. The model also does not explicitly account for source to source interactions, such as aftershocks. *Dieterich* [1994] demonstrated that the model does predict Omori decay in seismicity following a rapid change in stress (see equation (15)); however, because a nucleation-only theory cannot predict magnitudes, the current model cannot explicitly account for daughter events. A fully rigorous model, including dynamic rupture propagation would need to include the (potentially highly heterogeneous) initial stress and detailed fault geometry into account. This is beyond the domain of all but a few specialized calculations.

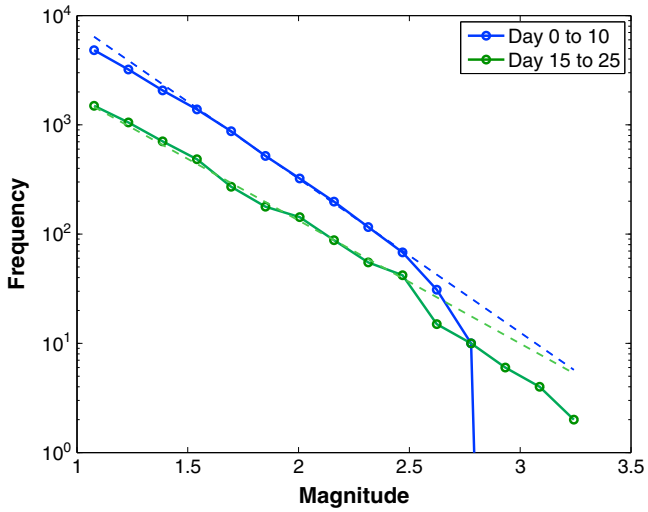

Figure 18. Frequency-magnitude distribution for simulated events shown in Figure 17. Events from the interval $0 < t < 10$ days, prior to shut-in shown in blue, post shut-in ($15 < t < 25$) are in green. Dashed lines show fits at intermediate magnitude.

Our model, while simplified, makes testable predictions. To the degree that assumption of homogeneously distributed sources and low background shear stress are met, we would anticipate a time-varying change in the frequency-magnitude distribution, as in Figure 16. *Bachmann et al.* [2011, Figure 4] show an apparent rollover in the frequency-magnitude distribution above $M \sim 2$ for coinjection seismicity at Basel; the rollover is at least shifted to larger magnitude in the postinjection period. Not surprisingly, the rate of small earthquakes is greater during injection. The slope of the frequency-magnitude relationship is also steeper during injection; $b = 1.6$ during injection versus 1.1 postinjection. We compare that with the simulation shown in Figure 17. Figure 18 compares the frequency-magnitude statistics for the first 10 days of injection to the first 10 days postinjection. The simulation exhibits all the features of the Basel data, although the details of course do not match: (1) the coinjection distribution rolls over at a lower magnitude than the postinjection data, (2) the rate of small earthquakes is higher during injection, and (3) the apparent b value is lower during injection ($b = 1.4$) compared to postinjection ($b = 1.1$). This suggests that the model is at least capturing some aspects of induced seismicity.

As noted above, *Bachmann et al.* [2011] find that postinjection seismicity at Basel decays following Omori's law. We illustrate the corresponding behavior for the simulation in Figure 19. The decay is roughly linear in log-log space at early times, with the curve flattening at later time as the seismicity decays to the background rate.

A surprising prediction of the model is that, under appropriate circumstances, the local seismicity rate can actually increase following shut-in. This is clearly something to look for in injection-induced seismicity. To be consistent with the poroelastic triggering mechanism, the geometry of the faults (orientation and slip vector) should be of the sense that injection-induced stresses *inhibit* slip. This is true for NS oriented normal faults (in the x_1 direction). For NS oriented reverse faults poroelastic stresses promote slip during injection (in the x_1 direction) but would inhibit slip in the postinjection period. Appropriately oriented strike-slip faults could also exhibit enhanced stressing postinjection. For example, strike-slip faults with fault normal radial to the injector would experience compression during injection. Post shut-in relaxation of that compressive stress could promote seismicity. The conclusion that poroelastic stresses can destabilize faults in the postinjection period is independent of assumptions in the *Dieterich* [1994] model.

We have shown (Figure 13) that tapering the injection limits the postinjection increase in seismicity rate. However, extending the duration of injection increases the probability of triggering a larger event. More work will be required to determine the optimal strategy for tapering injection, should the post shut-in rate increase be verified by field observations.

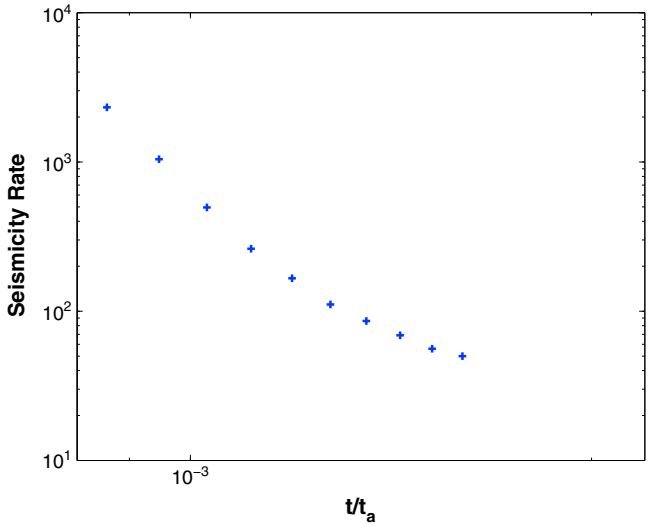

Figure 19. Decline in postinjection seismicity rate for simulated events shown in Figure 17. Log-log plot with time normalized by t_a.

10. Conclusions

1. For a homogeneous distribution of material properties and faults, poroelastic stresses are smaller than the direct pore pressure effect on fault strength. Nevertheless, because these stresses dominate over the pore pressure at large distances, they can have important dynamical consequences. Also, because seismicity rate depends exponentially on stress, coupling-induced stresses can change the predicted seismicity rate by orders of magnitude.
2. During injection poroelastic coupling may increase or decrease the seismicity rate, depending on the orientation of the faults relative to the injector. Coupling-induced stresses break the radial symmetry of the diffusion problem, leading to different seismicity rates in different azimuths, even for a uniform distributions of faults.
3. For constant injection flux, the time to reach a critical seismicity rate scales roughly with $t \sim r^2/(cf_c)$, where f_c is a factor that depends on frictional and poroelastic properties and r.
4. The model predicts that during injection seismicity rate decays with time following a peak, consistent with some observations. The decay depends both on hydraulic properties and the characteristic aftershock decay time t_a.
5. For finite duration injection at constant rate, shut-in leads to an outward propagating decrease in seismicity. However, if injection-induced stresses inhibit slip, abrupt shut-in can lead to locally sharp increase in the seismicity rate. Tapering the flux mitigates against the post shut-in spike in seismicity.
6. If the background ratio of shear to normal stress is sufficiently low, triggered ruptures may be confined to the volume perturbed by injection. This causes the seismicity rate of a given magnitude to depend both on the nucleation rate and the radius of the perturbed zone, which grows with $\sqrt{t}$. This leads to a rollover in the frequency-magnitude distribution for larger events, with a "corner magnitude" that increases with time.
7. Larger events are absent at short injection times but approach the background frequency with time. Larger events occurring post shut-in are thus not unexpected.
8. Our simulations exhibit frequency-magnitude statistics, comparing coinjection and postinjection periods qualitatively consistent with observations.
9. The simulated postinjection seismicity rate decays like Omori's law $(1/t)$ at short time, consistent with some observations, eventually merging into the background rate.

Appendix A: Stress Rates

The seismicity rate equations (12) require the stressing rates, which involve the time rate of change of both pore pressure and various stress components. We compute these as

$$\frac{\partial}{\partial t}\left(p(\boldsymbol{x},t)\right) = \frac{\partial}{\partial t}\left(\int_0^t f_p(\boldsymbol{x},t')\,\mathrm{d}t'\right) = \lim_{t'\to t^-} f_p(\boldsymbol{x},t') + \int_0^t \frac{\partial}{\partial t}\left(f_p(\boldsymbol{x},t')\right)\mathrm{d}t' \tag{A1}$$

$$\frac{\partial}{\partial t}\left(\sigma_{ij}(\boldsymbol{x},t)\right)=\frac{\partial}{\partial t}\left(\int_0^t f_{\sigma ij}(\boldsymbol{x},t')\,\mathrm{d}t'\right)=\lim_{t'\to t^-} f_{\sigma ij}(\boldsymbol{x},t')+\int_0^t \frac{\partial}{\partial t}\left(f_{\sigma ij}(\boldsymbol{x},t')\right)\mathrm{d}t', \tag{A2}$$

where $f_p(\boldsymbol{x},t')$ and $f_{\sigma ij}(\boldsymbol{x},t)$ are the integrands in equations (5) and (6). Consider first the limits. When $t'\to t^-$, $\xi(t')\to+\infty$, using L'Hôpital's rule: $g(\xi)\to 1$, $g'=\to 0$, $\xi g'\to 0$, such that

$$\lim_{t'\to t^-} f_p(\boldsymbol{x},t')=0 \tag{A3}$$

$$\lim_{t'\to t^-} f_{\sigma ij}(\boldsymbol{x},t')=\frac{q(t')\mu(\lambda_u-\lambda)}{2\pi\rho_0 r^3\alpha(\lambda_u+2\mu)}\left(\delta_{ij}-3\frac{x_i x_j}{r^2}\right). \tag{A4}$$

The time derivates of the integrands are

$$\frac{\partial}{\partial t}\left(f_p(\boldsymbol{x},t')\right)=\frac{q(t')(\lambda_u-\lambda)(\lambda+2\mu)}{(4\pi)^{\frac{3}{2}}\rho_0 r^3\alpha^2(\lambda_u+2\mu)}\left[\xi^2 e^{-\frac{1}{4}\xi^2}\left(3-\frac{1}{2}\xi^2\right)\right]\frac{\partial\xi}{\partial t} \tag{A5}$$

$$\frac{\partial}{\partial t}\left(f_{\sigma ij}(\boldsymbol{x},t')\right)=\frac{q(t')\mu(\lambda_u-\lambda)}{2\pi\rho_0 r^3\alpha(\lambda_u+2\mu)}\left[-\delta_{ij}\frac{d^2}{d\xi^2}g(\xi)+\frac{x_i x_j}{r^2}\left(\xi\frac{d^2}{d\xi^2}g(\xi)-2\frac{d}{d\xi}g(\xi)\right)\right]\frac{\partial\xi}{\partial t}, \tag{A6}$$

where ξ is given by (7). For the case of constant injection rate, the time derivatives of equations (9) and (10) are given by

$$\frac{\partial}{\partial t}\left(p(\boldsymbol{x},t)\right)=\frac{q(\lambda_u-\lambda)(\lambda+2\mu)}{8\pi^{\frac{3}{2}}\rho_0 r^3\alpha^2(\lambda_u+2\mu)}\xi^3 e^{-\frac{1}{4}\xi^2} \tag{A7}$$

$$\frac{\partial}{\partial t}\left(\sigma_{ij}(\boldsymbol{x},t)\right)=\frac{q(\lambda_u-\lambda)\mu}{8\pi\rho_0 r^3\alpha(\lambda_u+2\mu)}\left\{\delta_{ij}\left[-\frac{2}{\sqrt{\pi}}\xi^3 e^{-\frac{1}{4}\xi^2}+4g(\xi)\right]+\frac{x_i x_j}{r^2}\left[\frac{2}{\sqrt{\pi}}\xi^3 e^{-\frac{1}{4}\xi^2}-12g(\xi)\right]\right\}, \tag{A8}$$

where after integration over t', $\xi=r/\sqrt{ct}$.

Appendix B: Analytical Approximations

Making use of the definitions for Λ and the characteristic length scale r_q, in equation (18) we write the pore pressure change as

$$p(\boldsymbol{x},t)=\frac{r_q}{4\pi r}\Lambda\,\mathrm{erfc}\left(\frac{1}{2}\xi\right). \tag{B1}$$

Note that Λ has units of stress. Assuming that the Coulomb stress change is dominated by the pore pressure-induced change in effective stress *fp*, as in equation (17), at a critical level of seismicity R_c

$$\frac{a\bar{\sigma}}{f\Lambda}\frac{4\pi r}{r_q}\log(R_c)\approx\mathrm{erfc}\left(\frac{1}{2}\frac{r}{\sqrt{ct_c}}\right). \tag{B2}$$

Making use of the inverse of the erfc,

$$2\mathrm{erfc}^{-1}\left[\frac{a\bar{\sigma}}{f\Lambda}\frac{4\pi r}{r_q}\log(R_c)\right]\approx\frac{r}{\sqrt{ct_c}}, \tag{B3}$$

and rearranging

$$t_c\approx\frac{r^2}{c}\left\{2\mathrm{erfc}^{-1}\left[\frac{a\bar{\sigma}}{f\Lambda}\frac{4\pi r}{r_q}\log(R_c)\right]\right\}^{-2}\equiv\frac{r^2}{cf_c(r,R_c)}. \tag{B4}$$

The term in braces depends on *r* as well as injection rate and diffusivity.

To determine the range of validity of the approximation, note from (12) that the approximation breaks down when $\dot{\tau}/\dot{\tau}_0 \sim R$. We approximate $\dot{\tau} \approx f\dot{p}$. Thus, from (A7)

$$\frac{\dot{\tau}}{\dot{\tau}_0} \approx \frac{f\Lambda}{\dot{\tau}_0}\frac{q/\rho_0}{8\pi^{\frac{3}{2}}r^3}\xi^3 e^{-\frac{1}{4}\xi^2}. \tag{B5}$$

The normalized stressing rate (B5) equals R at a critical time that we label t_s, corresponding to $\xi_s = r/\sqrt{ct_s}$. Thus,

$$\frac{f\Lambda}{\dot{\tau}_0}\frac{q/\rho_0}{8\pi^{\frac{3}{2}}r^3}\xi_s^3 e^{-\frac{1}{4}\xi_s^2} \approx \exp\left[\frac{f\Lambda}{a\bar{\sigma}}\frac{r_q}{4\pi r}\mathrm{erfc}\left(\frac{1}{2}\xi_s\right)\right]. \tag{B6}$$

Taking logs of both sides,

$$\log\left[\frac{f\Lambda}{\dot{\tau}_0}\frac{q/\rho_0}{8\pi^{\frac{3}{2}}r^3}\right] + 3\log\xi_s - \frac{1}{4}\xi_s^2 \approx \frac{f\Lambda}{a\bar{\sigma}}\frac{r_q}{4\pi r}\mathrm{erfc}\left(\frac{1}{2}\xi_s\right). \tag{B7}$$

The critical time when the approximation breaks down is found from the roots ξ_s of (B7). The right-hand side is large only for small ξ; for small ξ the second and third terms on the left side are negligible. Thus, we neglect these terms and seek solutions of

$$\log\left[\frac{f\Lambda}{\dot{\tau}_0}\frac{q/\rho_0}{8\pi^{\frac{3}{2}}r^3}\right] \approx \frac{f\Lambda}{a\bar{\sigma}}\frac{r_q}{4\pi r}\mathrm{erfc}\left(\frac{1}{2}\xi_s\right) \tag{B8}$$

such that

$$\frac{a\bar{\sigma}}{f\Lambda}\frac{4\pi r}{r_q}\log\left(\frac{f\Lambda}{\dot{\tau}_0}\frac{q/\rho_0}{8\pi^{\frac{3}{2}}r^3}\right) \approx \mathrm{erfc}\left(\frac{1}{2}\xi_s\right) \tag{B9}$$

$$\frac{r}{\sqrt{ct_s}} \approx 2\mathrm{erfc}^{-1}\left[\frac{a\bar{\sigma}}{f\Lambda}\frac{4\pi r}{r_q}\log\left(\frac{f\Lambda}{\dot{\tau}_0}\frac{q/\rho_0}{8\pi^{\frac{3}{2}}r^3}\right)\right]. \tag{B10}$$

And finally,

$$t_s \approx \frac{r^2}{c}\left\{2\mathrm{erfc}^{-1}\left[\frac{a\bar{\sigma}}{f\Lambda}\frac{4\pi r}{r_q}\log\left(\frac{f\Lambda}{\dot{\tau}_0}\frac{q/\rho_0}{8\pi^{\frac{3}{2}}r^3}\right)\right]\right\}^{-2} \equiv \frac{r^2}{cf_s(r)}. \tag{B11}$$

Appendix C: Probability of Rupture Inside Perturbed Zone

In this section we compute the probability that an earthquake source, modeled as a circular crack of radius r_s, that has at least one point within a unit sphere lies entirely within that sphere. That probability is computed as the relative volume of all potential cracks that lie completely within the sphere to the volume of cracks that are at least tangent to the sphere.

Without loss of generality, take the z axis perpendicular to the crack planes and center the sphere at the coordinate origin. The crack center in the x, y plane is a distance r_c from the origin. At a given z ($-1 \le z \le 1$), a crack that has at least one point within the sphere must have its center, $r_c \le r(z) + r_s$, where $r(z) = \sqrt{1-z^2}$. The condition that the crack lie entirely within the sphere is $r_c \le r(z) - r_s$, (Figure C1).

The probability that a crack that at least partly lies within the unit sphere is entirely within that sphere is the ratio of volumes occupied by cracks that lie completely within the sphere to the volume occupied by cracks that are at least partly within the sphere,

$$P_{\mathrm{in}} = \frac{\pi\int_{-z_c}^{z_c}\left(\sqrt{1-z^2}-r_s\right)^2 \mathrm{d}z}{\pi\int_{-1}^{1}\left(\sqrt{1-z^2}+r_s\right)^2 \mathrm{d}z}, \tag{C1}$$

where $z_c = \sqrt{1-r_s^2}$. The integral in the numerator is over the domain $-z_c \le z \le z_c$, since disks of radius r_s do not fit within the sphere for $|z| > z_c$. The definite integrals in (C1) lead to

$$P_{in} = \frac{2\left[z_c - r_s\sin^{-1}(z_c) - \frac{z_c^3}{3}\right]}{2r_s^2 + \pi r_s + \frac{4}{3}}. \tag{C2}$$

P_{in} as a function of r_s/r is shown in Figure 14. We also tested (C2) against simulations where crack centers were randomly generated and the probability of those cracks lying completely within the unit sphere is shown in the figure.

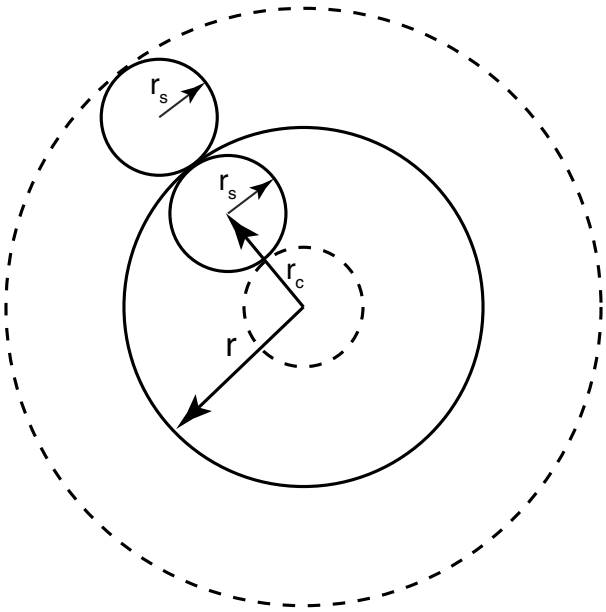

Figure C1. Diagram for determining the probability that a source disk with radius r_s lies completely within the perturbed volume. Radius of the perturbed zone at depth z is r, where $r(z) = \sqrt{1 - z^2}$. Let r_c designate the distance of the source center form the z-axis (origin in the figure). The condition that the crack lies entirely within the circle is $r_c \leq r - r_s$. The condition that at least one point lies within the circle is $r_c \leq r + r_s$.

Acknowledgments
Thanks to Andrew Bradley for assistance with computations, Jeff McGuire and Eric Dunham for discussion. We also thank reviewers Paul Hsieh and John Rudnicki for helpful comments that substantially improved the manuscript. Funding to S.-Y. L. provided by the Stanford Center for Induced and Triggered Seismicity. No data was used in producing this manuscript.

References

Ake, J., K. Mahrer, D. O'Connell, and L. Block (2005), Deep-injection and closely monitored induced seismicity at Paradox Valley, Colo., *Bull. Seismol. Soc. Am.*, *95*(2), 664–683.

Bachmann, C., S. Wiemer, J. Woessner, and S. Hainzl (2011), Statistical analysis of the induced Basel 2006 earthquake sequence: Introducing a probability-based monitoring approach for enhanced geothermal systems, *Geophys. J. Int.*, *186*(2), 793–807.

Baisch, S., R. Vörös, E. Rothert, H. Stang, R. Jung, and R. Schellschmidt (2010), A numerical model for fluid injection induced seismicity at Soultz-sous-Forêts, *Int. J. Rock Mech. Min. Sci.*, *47*(3), 405–413.

Barth, A., F. Wenzel, and C. Langenbruch (2013), Probability of earthquake occurrence and magnitude estimation in the post shut-in phase of geothermal projects, *J. Seismol.*, *17*(1), 5–11.

Biot, M. A. (1941), General theory of 3-dimensional consolidation, *J. Appl. Phys.*, *12*, 155–164.

Deichmann, N., and D. Giardini (2009), Earthquakes induced by the stimulation of an enhanced geothermal system below Basel (Switzerland), *Seismol. Res. Lett.*, *80*(5), 784–798.

Dieterich, J. (1994), A constitutive law for rate of earthquake production and its application to earthquake clustering, *J. Geophys. Res.*, *99*(B2), 2601–2618.

Dieterich, J. H., and B. Kilgore (1996), Implications of fault constitutive properties for earthquake prediction, *Proc. Natl. Acad. Sci.*, *93*(9), 3787–3794.

Dorbath, L., N. Cuenot, A. Genter, and M. Frogneux (2009), Seismic response of the fractured and faulted granite of Soultz-sous-Forêts (France) to 5 km deep massive water injections, *Geophys. J. Int.*, *177*(2), 653–675.

Eaton, D. W., J. Davidsen, P. K. Pedersen, and N. Boroumand (2014), Breakdown of the Gutenberg-Richter relation for microearthquakes induced by hydraulic fracturing: Influence of stratabound fractures, *Geophys. Prospect.*, *62*(4), 806–818.

Ellsworth, W. L. (2013), Injection-induced earthquakes, *Science*, *341*(6142), 1,225,942, doi:10.1126/science.1225942.

Hart, D. J., and H. F. Wang (1995), Laboratory measurements of a complete set of poroelastic moduli for Berea sandstone and Indiana limestone, *J. Geophys. Res.*, *100*(B9), 17,741–17,751.

Healy, J., W. Rubey, D. Griggs, and C. Raleigh (1968), The Denver earthquakes, *Science*, *161*, 1301–1310.

Horton, S. (2012), Disposal of hydrofracking waste fluid by injection into subsurface aquifers triggers earthquake swarm in central Arkansas with potential for damaging earthquake, *Seismol. Res. Lett.*, *83*(2), 250–260.

Hsieh, P. A., and J. D. Bredehoeft (1981), A reservoir analysis of the Denver earthquakes: A case study of induced seismicity, *J. Geophys. Res.*, *86*, 903–920.

Keranen, K., M. Weingarten, G. Abers, B. Bekins, and S. Ge (2014), Sharp increase in central Oklahoma seismicity since 2008 induced by massive wastewater injection, *Science*, *345*(6195), 448–451.

Kim, W.-Y. (2013), Induced seismicity associated with fluid injection into a deep well in Youngstown, Ohio, *J. Geophys. Res. Solid Earth*, *118*(7), 3506–3518, doi:10.1002/jgrb.50247.

Marone, C. (1998), Laboratory-derived friction laws and their application to seismic faulting, *Ann. Rev. Earth Planet. Sci.*, *26*, 643–696.

Noda, H., E. M. Dunham, and J. R. Rice (2009), Earthquake ruptures with thermal weakening and the operation of major faults at low overall stress levels, *J. Geophys. Res.*, *114*, B07302, doi:10.1029/2008JB006143.

National Research Council (2013), *Induced Seismicity Potential in Energy Technologies*, National Acad. Press, Washington, D. C.

Raleigh, C., J. Healy, and J. Bredehoeft (1976), An experiment in earthquake control at Rangely, Colorado, *Science*, *191*, 1230–1237.

Rice, J. R. (2006), Heating and weakening of faults during earthquake slip, *J. Geophys. Res.*, *111*, B05311, doi:10.1029/2005JB004006.

Rice, J. R., and M. Cleary (1976), Some basic stress diffusion solutions for fluid-saturatedelastic porous media with compressible constituents, *Rev. Geophys.*, *14*, 227–241.

Rozhko, A. Y. (2010), Role of seepage forces on seismicity triggering, *J. Geophys. Res.*, *115*, B11314, doi:10.1029/2009JB007182.
Rudnicki, J. W. (1986), Fluid mass sources and point forces in linear elastic diffusive solids, *Mech. Mater.*, *5*(4), 383–393.
Rutqvist, J., J. Birkholzer, and C.-F. Tsang (2008), Coupled reservoir-geomechanical analysis of the potential for tensile and shear failure associated with CO_2 injection in multilayered reservoir-caprock systems, *Int. J. Rock Mech. Min. Sci.*, *45*(2), 132–143.
Segall, P. (1989), Earthquakes triggered by fluid extraction, *Geology*, *17*, 942–946.
Segall, P. (2010), *Earthquake and Volcano Deformation*, 432 pp., Princeton Univ. Press, N. J.
Segall, P., J. R. Grasso, and A. Mossop (1994), Poroelastic stressing and induced seismicity near the Lacq gas field, *J. Geophys. Res.*, *99*(B8), 15,423–15,438.
Shapiro, S. A., E. Huenges, and G. Borm (1997), Estimating the crust permeability from fluid-injection-induced seismic emission at the KTB site, *Geophys. J. Int.*, *131*(2), F15–F18.
Shapiro, S. A., E. Rothert, V. Rath, and J. Rindschwentner (2002), Characterization of fluid transport properties of reservoirs using induced microseismicity, *Geophysics*, *67*(1), 212–220, doi:10.1190/1.1451597.
Shapiro, S. A., O. S. Krüger, and C. Dinske (2013), Probability of inducing given-magnitude earthquakes by perturbing finite volumes of rocks, *J. Geophys. Res. Solid Earth*, *118*, 3557–3575, doi:10.1002/jgrb.50264.
Suckale, J. (2009), Induced seismicity in hydrocarbon fields, *Adv. Geophys.*, *51*, 55–106.
Wang, H. (2000), *Theory of Linear Poroelasticity With Applications to Geomechanics and Hydrogeology*, Princeton Univ. Press, Princeton, N. J.
Zhang, Y., et al. (2013), Hydrogeologic controls on induced seismicity in crystalline basement rocks due to fluid injection into basal reservoirs, *Groundwater*, *51*(4), 525–538.